Biophysical Journal, Volume 98

Supporting Material

A Multiscale Model of Venous Thrombus Formation with Surface-Mediated Control of Blood Coagulation Cascade

Zhiliang Xu, Joshua Lioi, Jian Mu, Malgorzata Kamocka, Xiaomin Liu, Danny Chen, Elliot Rosen, and Mark Alber

Supporting Material

1 Discrete stochastic cellular Potts model (CPM)

Stochastic discrete models are used in a variety of problems dealing with biological complexity. One motivation for this approach is the enormous range of length scales of typical biological phenomena. Treating cells as simplified interacting agents, one can simulate the interactions of tens of thousands to millions of cells and still have within reach the smaller-scale structures of tissues and organs that would be ignored in continuum (e.g., partial differential equation) approaches. At the same time, discrete stochastic models can be made sophisticated enough to reproduce almost all commonly observed types of cell behavior (2, 3, 5, 7, 8, 13, 14).

In the CPM each cell consists of many lattice sites (pixels). Distribution of multidimensional indices associated with lattice cites determines current system configuration. The effective energy of the system mixes true energies, like cell-cell and cell-injury adhesions, and terms that mimic energies, e.g., the response of a cell to a blood flow and area or volume constraint

$$E = E_{Adhesion} + E_{Area} + E_{Chemical}. \tag{1.1}$$

Given an effective energy one cell motion is calculated using Metropolis dynamics algorithm based on the Monte-Carlo Boltzmann acceptance rule (11). Namely, if a proposed change in lattice configuration (*i.e.* a change of the index associated with a pixel) changes the effective energy by ΔE, the change is accepted with probability:

$$P(\Delta E) = \begin{cases} 1, & \Delta E \leq 0 \\ e^{-\frac{\Delta E}{T}} & \Delta E > 0, \end{cases} \tag{1.2}$$

where T, defined in units of energy, determines effective cell membrane fluctuation amplitude and is estimated based on the value of ΔE, to be between $0.2 \leq \Delta E/T \leq 2.0$ (1). The pattern of pixels with the same index evolves (and cell moves) to minimize the total effective energy.

In the blood clot model, inactivated platelets and blood cells are introduced from the inlet on the left side at a specified rate and move to the right. When cells reach the right side of the simulation domain, they are removed from the system. The "no-flux" boundary conditions are imposed on both upper and lower boundaries so that cells would not move outside of the domain.

On each CPM iteration step a lattice site (pixel) is randomly chosen and change of its index (state) is attempted. System energy change is calculated and the probability of its acceptance is determined. Generator of random numbers is used to determine which index to implement. This is followed by adjustment of the lattice site index and update of the

corresponding cell properties (cell size, cell boundary position and cell type). For a given CPM lattice of the size $(m \times n)$, one Monte Carlo Step (MCS) of a simulation consists of $(m \times n)$ attempts at index changes of randomly chosen lattice cites. When an inactivated platelet reaches the site of the injury or region with IIa concentration higher than the set threshold value (1nM), it changes its type to "activated" and starts coagulation process on its surface.

We further extended the CPM sub-model to take the volume shrinkage of activated platelets into consideration. In this extension, a platelet has two prescribed target volumes ν_1 and ν_2 depending on its biological status. Here ν_1 is the volume of a platelet at the resting state; and ν_2 is the target volume of activated platelets flatten out to form more spherical structures with developing filipodia, which is about 20% of ν_1. (Remark: In real experiments, the volume of a platelet shrinks to approximately 10% of its original one. We use 20% only for the stability of the algorithm. In CPM sub-model, if the number of pixels of a cell is too few, the cell will be deleted.) This process of volume shrinking takes about three minutes. We assume a linear relation between ν_1 and ν_2. Therefore the intermediate volume $\nu(t)$ is prescribed by

$$\nu(t) = \begin{cases} \nu_1(1.0 - \frac{t}{180.0}\left(\frac{4}{5}\right)), & t \leq 180 \\ 0.2\nu_1 & t > 180, \end{cases} \tag{1.3}$$

where t is the time that a platelet being activated.

Coupling time scales of continuous models and CPM: The CPM is an extension of the Potts model which does not explicitly indicate its physical time scale. The time scale is imposed on the CPM by matching the simulated dynamics with the real physical one. The time scale between the CPM and the continuous model is established by matching the simulated platelet velocity with the blood flow velocity calculated from the Navier-Stokes equation. During the parameter calibration process, we gradually adjust the flow energy constant in the CPM until the platelet velocity matches that of the blood flow. Table 1 lists typical PM parameter values used for simulations described in the paper.

2 Image analysis of venous thrombi formation

A connection between biological experiments and model simulations has been established by using newly developed image segmentation, reconstruction, and analysis algorithms (9, 10). A venous blood thrombus (clot) is generally composed of platelets and fibrin/fibrinogen. It may also incorporate other blood cells (leukocytes and red blood cells) during its development. In a 3-dimensional microscopic image, the clot is seen as a cluster of voxels with certain fluorescent signals. Specifically, in Fogure 1 *blue* signal represents plasma (dextran), *green* is for fibrinogen/fibrin, *red* is for platelets, and *black* is for everything else (i.e., excluding the three fluorescently tagged components). Therefore, the image processing task is to identify and analyze the structures (or shapes) formed by red and green voxels plus the surrounding "black" voxels (for other blood cells) in 3D images.

The information for each voxel actually consists of three values (called *channels*), representing the levels of red, green, and blue (each from 0 to 255). Hence, there are possibly many different combinations of channel values for each voxel. In the 3D clot images fibrin and platelets (or red and green voxels) cluster together to form clots. While there are clusters of red and green points, the 3D space is also filled with many other red and green points.

Table 1: Parameter values for simulations of the thrombus development.

Flow Parameters	
Finite difference grid	210×60
Inlet Pressure	1 bar
Plasma Viscosity	0.015
Inlet Velocity **u**	(500, 0) μm/s
Domain Size	280μm×80μm
Simulation time	30 sec.
CPM parameters	
CPM grid	1050×300
Fluctuation temperature T	10
Adhesion const. J	
blood-platelets	18.0
quiescent platelet-quiescent platelets	20.0
activated platelet-activated platelets	8.0
activated platelet-injury	2.0
activated platelet-vessel wall	18.0
Target volume v_{target} platelet	30
Target volume v_{target} blood cell	100
Volume const. λ	2.0
Volume const. λ'	0.0
Fluid const. K_{e1}	25.0
Fluid const. K_{e2}	0.2
Threshold 1	0.4
Threshold 2	1.0
Fibrin production rate. κ	1.0
Time-steps	20 CPM steps per NS step, 1050×300 trials per CPM steps
Coagulation reaction parameters	Parameters are the same as in (17, 18, 19)

Thus, the image analysis problem is to first identify the clusters (or galaxies) of discrete red or green points or voxels while at the same time ignore the "isolated" red or green points (or isolated stars). Then obtained clusters can be used for reconstructing surfaces and calculating volumes of the clots. Therefore, a clot is defined as a maximal set of density-connected voxels and can be obtained using density-based clustering (DBC) algorithm (4).

The clot identification algorithm consists of the following main steps.

(1) Image intensification: modify (i.e., increase or decrease) the channel values of each voxel based on a functional mapping, such that those voxels with high red or green channel values have a bigger chance of being classified as red or green voxels, and those voxels with low red or green channel values have a higher chance to be ignored.

(2) Threshold determination: apply Otsu's method (12) to compute threshold value for each of the three channels for every 2D image slice in the 3D image. The idea of Otsu's method is to search for the threshold that minimizes the in-class variance and maximizes the between-class variance.

(3) Voxel classification: classify each voxel v of every 2D image slice as follows. Find the maximum value among the three channels of v (say, this value is red); if this red value is above the threshold of that slice for red, then v is classified as a red voxel; otherwise, v is a black voxel.

(4) Density-based clustering: determine clusters of maximal density-connected red or green voxels in the 3D image.

(5) Blood cell inclusion: add the surrounding black voxels (i.e., other blood cells) of each cluster to the image of the clot.

Estimation of porosity. Our image identification algorithms show that volume of a typical blood clot resulting from vessel injury in a wild-type mice increases rapidly at an earlier time and then shrinks dramatically soon after reaching its peak. Then the size of the blood clot becomes relatively stable and does not change much. To monitor the growth of a clot, we produced a complete sequence of 3D images for a sequence of time points with an interval between two consecutive points being forty seconds. We focus on three typical time points in experiments corresponding to clot starting to grow, its volume peaking, and its size stabilizing. In the clot image sequence, these three time points correspond to the first, second, and sixth 3D images labeled as T1, T2 and T3 in Table 2.

Without further differentiating components of a clot, for each time point, we produce from the 3D image a list of 2D binary image slices each represented by a 3D matrix. The 3D binary image separates all voxels into two classes: clot and non-clot. Each cell in the matrix corresponds to one voxel in the binary image, where 1 means that the voxel belongs to the clot, and 0 otherwise. We use a percentage indicating the proportion of void (i.e., non-clot) space in a rectangular cuboid region which is entirely contained in the clot to measure the porosity of the clot. This percentage represents the ratio of the total volume of the void space to the total volume of the region (including both clot and void voxels). To ensure the robustness of the percentage value, after we select the initial position of the "box" (i.e.,

Table 2: Clot porosity at three different time points

Sample no.	T1	Porosity (%)	T2	Porosity (%)	T6	Porosity (%)
1	59325	20.90	63333	15.56	69012	7.98
2	57746	23.00	63794	14.94	69581	7.23
3	58120	22.51	64041	14.61	68837	8.22
4	58901	21.47	64183	14.42	68540	8.61
5	58311	22.25	64370	14.17	69904	6.79
6	58019	22.64	64494	14.01	69331	7.56
7	57908	22.79	64450	14.07	68799	8.27
8	57899	22.80	64323	14.24	68736	8.35
9	58062	22.58	64139	14.48	69012	7.98
10	57803	22.93	63916	14.78	69538	7.28

cuboid region), we gradually move the box around to check how consistent this ratio value is in nearby locations. Specifically, we move the box of the size: $30\times50\times50$ along certain directions and use a step length of 2 for each box size, resulting in 10 sample values. During the process of moving the box around, we maintain the same box size and make sure that the entire box is always inside the clot. Then we count the number of clot voxels inside the box and calculate the porosity value. Table 2 shows some of the obtained porosity values. Unless other specified, we choose in the paper an average value $\cong 0.15$ for porosity in our simulations.

Number of platelets in the middle slice of a clot. Since our model is 2D, we effectively compare simulations with an image of a middle slice of a clot. To justify the number of platelets used in the simulations (from 10^2 to 1000), we counted the number of platelets within individual slices obtained from the experiments using the image analysis technique described above. In our image setting, the size of a voxel in a 3D image is $0.44^3 \times 10^{-9}$ mm^3. A typical clot at the stabilized stage usually consists of about 5×10^5 voxels. Thus, the typical size of a clot is around 4.26×10^{-5} mm^3. The total number of pixels that are labeled and classified as of the platelet type is usually in the range of $(2000, 4000)$. The ratio of the number of platelet pixels over the number of platelets is approximately 5/1. Therefore, the total number of platelets in the slice is in the range of $(400, 800)$, which is consistent with the number used in the simulations. Figure 1 provides examples of images of a 2D slice of the same experimental wild type clot together with corresponding numbers of platelets, at different time points. In this example, the platelet number of the slice at one time point is a little beyond the "usual" range of platelet numbers because the size of the clot is larger than the "average" ones.

3 Discussion of the role of protein C

One potential problem with modeling the role of protein C in clot formation is that it is not obvious where APC is generated in a developing thrombus since aggregating platelets are not likely to expose TM. TM is exposed on a resting endothelium. It is unlikely that PC plays a role in protecting the endothelium following laser induced injury. However, PC

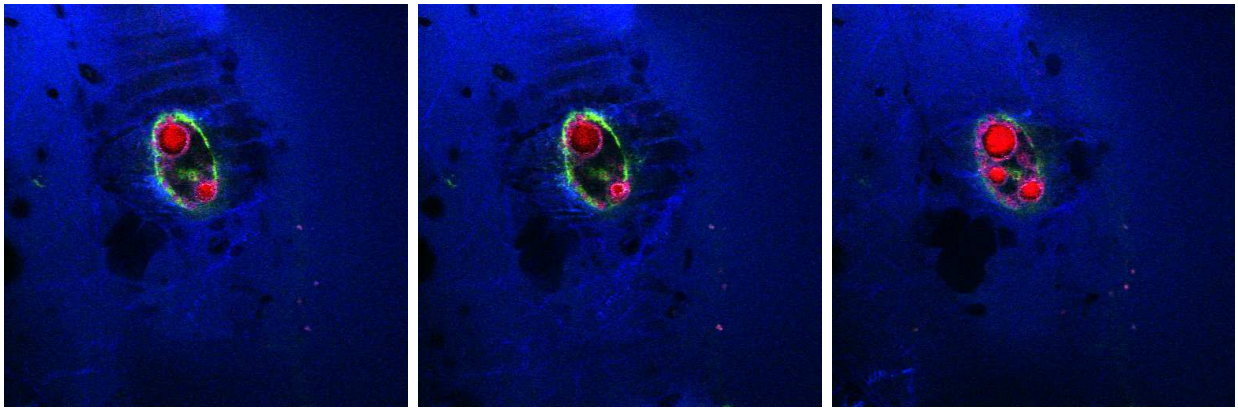

(a) (b) (c)

Figure 1: Images of the same slice in the middle of a wild type clot at different time points. (a) The number of platelets = 695 (6 minutes after injury); (b) the number of platelets = 897 (6 minutes 40 seconds after injury); (c) the number of platelets = 1231 (7 minutes 20 seconds after injury).

might block activation of endothelium adjacent to the injury site. It is also unlikely that undamaged endothelium upstream are the site of APC generation, since it is unlikely that a significant amount of thrombin generated in the thrombus will diffuse upstream against blood flow. Conceivably, thrombin reaches TM exposed on endothelium downstream, but similarly it is not clear how the APC reaches the thrombus by diffusion upstream against the flow. Therefore, it is hypothesized that APC production occurs on the endothelial cells in the lateral direction of the injury.

4 Coagulation sub-model

4.1 Model equations

Notations:
$\frac{d[\,]}{dt}$ - ordinary time derivative of concentration for certain chemical;
$\frac{\partial[\,]}{\partial t}$ - partial time derivative of concentration for certain chemical;
$[TF]$ - concentration of tissue factor;
$[VII]$ - concentration of factor 7 in blood flow;
$[VII_a]$ - concentration of activated factor 7 in blood flow;
$[X^m]$ - concentration of factor 10 binded to the platelet surface;
$[TF:VII_a]$ - concentration of tissue factor and activated factor 7 complex.

$$\frac{d[TF]}{dt} = -k_2[TF][VII] + k_1[TF:VII] - k_4[TF][VII_a] + k_3[TF:VII_a] \tag{4.1}$$

$$\begin{aligned}\frac{\partial[VII]}{\partial t} + \mathbf{u}\cdot\nabla[VII] = \; & D_{VII}\nabla^2[VII] - k_2[TF][VII] + k_1[TF:VII^m] - \\ & k_5[TF:VII_a^m][VII] - k_6[X_a][VII] - k_7[II_a][VII]\end{aligned} \tag{4.2}$$

$$\frac{d[TF:VII^m]}{dt} = k_2[TF][VII] - k_1[TF:VII^m] \tag{4.3}$$

$$\begin{aligned}\tfrac{\partial[VII_a]}{\partial t} + \mathbf{u}\cdot\nabla[VII_a] = \;& D_{VII_a}\nabla^2[VII_a] - k_4[TF][VII_a] + k_3[TF:VII_a^m] + \\ & k_5[TF:VII_a^m][VII] + k_6[X_a][VII] + k_7[II_a][VII]\end{aligned} \tag{4.4}$$

$$\begin{aligned}\tfrac{d[TF:VII_a^m]}{dt} = \;& k_4[TF][VII_a] - k_3[TF:VII_a^m] - k_9[TF:VII_a^m][X] \\ & + k_8[TF:VII_a^m:X] - k_{12}[TF:VII_a^m][X_a] + k_{11}[TF:VII_a^m:X_a] - \\ & k_{14}[TF:VII_a^m][IX] + k_{13}[TF:VII_a^m:IX] - \\ & k_{37}[TF:VII_a^m][X_a:TFPI] - \\ & k_{42}[TF:VII_a^m][ATIII] + k_{15}[TF:VII_a^m:IX]\end{aligned} \tag{4.5}$$

$$\begin{aligned}\tfrac{\partial[X_a]}{\partial t} + \mathbf{u}\cdot\nabla[X_a] = \;& D_{X_a}\nabla^2[X_a] - k_{10}^{on}[X_a](p_{10} - e_{10}^{mtot} - z_{10}^{mtot}) + k_{10}^{off}[X_a^m] - \\ & k_{12}[TF:VII_a][X_a] + k_{11}[TF:VII_a:X_a] - k_{34}[X_a][TFPI] + \\ & k_{33}[X_a:TFPI] - k_{38}[X_a][ATIII]\end{aligned} \tag{4.6}$$

$$\begin{aligned}\tfrac{\partial[II_a]}{\partial t} + \mathbf{u}\cdot\nabla[II_a] = \;& D_{II_a}\nabla^2[II_a] - k_2^{on}[II_a](p_2 - e_2^{mtot} - z_2^{mtot}) + k_2^{off}[II_a^m] \\ & - k_{41}[II_a][ATIII] \\ & - D_{(diff,II_a^{EC})}([II_a] - [II_a^{EC}])\end{aligned} \tag{4.7}$$

$$\begin{aligned}\tfrac{\partial[X]}{\partial t} + \mathbf{u}\cdot\nabla[X] = \;& D_X\nabla^2[X] - k_{10}^{on}[X](p_{10} - e_{10}^{mtot} - z_{10}^{mtot}) + \\ & k_{10}^{off}[X^m] - k_9[TF:VII_a][X] + (k_{10} + k_8)[TF:VII_a:X]\end{aligned} \tag{4.8}$$

$$\tfrac{d[TF:VII_a^m:X]}{dt} = k_9[TF:VII_a^m][X] - k_{10}[TF:VII_a^m:X] - k_8[TF:VII_a^m:X] \tag{4.9}$$

$$\begin{aligned}\tfrac{d[TF:VIIa^m:X_a]}{dt} = \;& k_{12}[TF:VII_a^m][X_a] - k_{11}[TF:VII_a^m:X_a] + k_{10}[TF:VII_a^m:X] \\ & - k_{36}[TF:VII_a^m:X_a][TFPI] + k_{35}[TF:VII_a^m:X_a:TFPI]\end{aligned} \tag{4.10}$$

$$\begin{aligned}\tfrac{\partial[IX]}{\partial t} + \mathbf{u}\cdot\nabla[IX] = \;& D_{IX}\nabla^2[IX] - k_9^{on}[IX](p_9 - e_9^{mtot} - z_9^{mtot}) + k_9^{off}[IX^m] \\ & - k_{14}[TF:VII_a][IX] + k_{13}[TF:VII_a:IX]\end{aligned} \tag{4.11}$$

$$\begin{aligned}\tfrac{d[TF:VII_a^m:IX]}{dt} = \;& k_{14}[TF:VII_a^m][IX] - k_{15}[TF:VII_a^m:IX] \\ & - k_{13}[TF:VII_a^m:IX]\end{aligned} \tag{4.12}$$

$$\begin{aligned}\tfrac{\partial[IX_a]}{\partial t} + \mathbf{u}\cdot\nabla[IX_a] = \;& D_{IX_a}\nabla^2[IX_a] - k_9^{on}[IX_a](p_9 - e_9^{mtot} - z_9^{mtot}) + k_9^{off}[IX_a^m] \\ & + k_{25}[IX_a:VIII_a:X^m] + -k_{40}[IX_a][ATIII] + \\ & k_{15}[TF:VII_a^m:IX]\end{aligned} \tag{4.13}$$

$$\frac{\partial[II]}{\partial t} + \mathbf{u} \cdot \nabla[II] = D_{II}\nabla^2[II] - k_2^{on}[II](p_2 - e_2^{mtot} - z_2^{mtot}) \quad + k_2^{off}[II^m] \tag{4.14}$$

$$\begin{aligned}\frac{\partial[VIII]}{\partial t} + \mathbf{u} \cdot \nabla[VIII] = \quad & D_{VIII}\nabla^2[VIII] - k_8^{on}[VIII](p_8 - e_8^{mtot} - z_8^{mtot}) + k_8^{off}[VIII^m] \\ & -k_{17}[II_a][VIII]\end{aligned} \tag{4.15}$$

$$\begin{aligned}\frac{\partial[VIII_a]}{\partial t} + \mathbf{u} \cdot \nabla[VIII_a] = \quad & D_{VIII_a}\nabla^2[VIII_a] - k_8^{on}[VIII_a](p_8 - e_8^{mtot} - z_8^{mtot}) + \\ & k_8^{off}[VIII_a^m] + k_{17}[II_a][VIII] - k_{24}[VIII_a] \\ & +k_{23}[VIII_{a1}L][VIII_{a2}]\end{aligned} \tag{4.16}$$

$$\begin{aligned}\frac{d[IX_a{:}VIII_a]}{dt} = \quad & k_{19}[VIII_a][IX_a] - k_{18}[IX_a : VIII_a] - k_{21}[IX_a : VIII_a][X] + \\ & k_{20}[IX_a : VIII_a : X] - k_{25}[IX_a : VIII_a] + k_{22}[IX_a : VIII_a : X]\end{aligned} \tag{4.17}$$

$$\begin{aligned}\frac{d[IX_a{:}VIII_a{:}X^m]}{dt} = \quad & k_{21}[IX_a : VIII_a][X^m] - k_{20}[IX_a : VIII_a : X^m] - \\ & k_{22}[IX_a : VIII_a : X^m] - k_{25}[IX_a : VIII_a : X^m]\end{aligned} \tag{4.18}$$

$$\begin{aligned}\frac{\partial[VIII_{a1}L]}{\partial t} + \mathbf{u} \cdot \nabla[VIII_{a1}L] = \quad & D_{VIII_{a1}L}\nabla^2[VIII_{a1}L]k_{24}[VIII_a] - k_{23}[VIII_{a1}L][VIII_{a2}] + \\ & k_{25}[IX_a : VIII_a : X] + k_{25}[IX_a : VIII_a]\end{aligned} \tag{4.19}$$

$$\begin{aligned}\frac{\partial[VIII_{a2}]}{\partial t} + \mathbf{u} \cdot \nabla[VIII_{a2}] = \quad & D_{VIII_{a2}}\nabla^2[VIII_{a2}]k_{24}[VIII_a] - k_{23}[VIII_{a1}][VIII_{a2}] \\ & +k_{25}[IX_a : VIII_a : X] + k_{25}[IX_a : VIII_a]\end{aligned} \tag{4.20}$$

$$\begin{aligned}\frac{\partial[V]}{\partial t} + \mathbf{u} \cdot \nabla[V] = \quad & D_V\nabla^2[V] - k_5^{on}[V](p_5 - e_5^{mtot} - z_5^{mtot}) + k_5^{off}[V^m] \\ & -k_{26}[II_a][V]\end{aligned} \tag{4.21}$$

$$\begin{aligned}\frac{\partial[V_a]}{\partial t} + \mathbf{u} \cdot \nabla[V_a] = \quad & D_{V_a}\nabla^2[V_a] - k_5^{on}[V_a](p_5 - e_5^{mtot} - z_5^{mtot}) + k_5^{off}[V_a^m] \\ & +k_{26}[II_a][V]\end{aligned} \tag{4.22}$$

$$\begin{aligned}\frac{d[X_a{:}V_a]}{dt} = \quad & k_{28}[X_a^m][V_a^m] - k_{27}[X_a : V_a] - k_{30}[X_a : V_a][II^m] + k_{31}[X_a : V_a : II^m] \\ & +k_{29}[X_a : V_a : II^m]\end{aligned} \tag{4.23}$$

$$\frac{d[X_a{:}V_a{:}II^m]}{dt} = k_{30}[X_a : V_a][II^m] - k_{29}[X_a : V_a : II^m] - k_{31}[X_a : V_a : II^m] \tag{4.24}$$

$$\frac{\partial[mII_a]}{\partial t} + \mathbf{u}\cdot\nabla[mII_a] = \begin{array}{l} D_{mII_a}\nabla^2[mII_a] - k_2^{on}[mII_a](p_2 - e_2^{mtot} - z_2^{mtot}) + k_2^{off}[mII_a^m] \\ -k_{39}[mII_a][ATIII] \end{array} \tag{4.25}$$

$$\frac{\partial[TFPI]}{\partial t} + \mathbf{u}\cdot\nabla[TFPI] = \begin{array}{l} D_{TFPI}\nabla^2[TFPI] - k_{34}[X_a][TFPI] + k_{33}[X_a:TFPI] \\ -k_{36}[TF:VII_a:X_a][TFPI] + k_{35}[TF:VII_a:X_a:TFPI] \end{array} \tag{4.26}$$

$$\frac{\partial[X_a{:}TFPI]}{\partial t} + \mathbf{u}\cdot\nabla[X_a:TFPI] = \begin{array}{l} D_{X_a:TFPI}\nabla^2[X_a:TFPI]k_{34}[X_a][TFPI] \\ -k_{33}[X_a:TFPI] - k_{37}[TF:VII_a][X_a:TFPI] \end{array} \tag{4.27}$$

$$\frac{d[TF{:}VII_a^m{:}X_a{:}TFPI]}{dt} = \begin{array}{l} k_{36}[FT:VII_a^m:X_a][TFPI] - \\ k_{35}[TF:VII_a^m:X_a:TFPI] + \\ k_{37}[TF:VII_a^m][X_a:TFPI] \end{array} \tag{4.28}$$

$$\frac{\partial[ATIII]}{\partial t} + \mathbf{u}\cdot\nabla[ATIII] = \begin{array}{l} D_{ATIII}\nabla^2[ATIII] - k_{38}[X_a][ATIII] - k_{39}[mII_a][ATIII] - \\ k_{40}[IX_a][ATIII] - k_{41}[II_a][ATIII] - k_{42}[TF:VII_a][ATIII] \end{array} \tag{4.29}$$

$$\frac{\partial[X_a{:}ATIII]}{\partial t} + \mathbf{u}\cdot\nabla[X_a:ATIII] = D_{\mathrm{X_a:ATIII}}\nabla^2[X_a:ATIII] + k_{38}[X_a][ATIII] \tag{4.30}$$

$$\frac{\partial[mII_a{:}ATIII]}{\partial t} + \mathbf{u}\cdot\nabla[mII_a:ATIII] = D_{\mathrm{mII_a:ATIII}}\nabla^2[mII_a:ATIII] + k_{39}[mII_a][ATIII] \tag{4.31}$$

$$\frac{\partial[IX_a{:}ATIII]}{\partial t} + \mathbf{u}\cdot\nabla[IX_a:ATIII] = D_{\mathrm{IX_a:ATIII}}\nabla^2[IX_a:ATIII] + k_{40}[IX_a][ATIII] \tag{4.32}$$

$$\frac{\partial[II_a{:}ATIII]}{\partial t} + \mathbf{u}\cdot\nabla[II_a:ATIII] = D_{\mathrm{II_a:ATIII}}\nabla^2[II_a:ATIII]k_{41}[II_a][ATIII]\ ll \tag{4.33}$$

$$\frac{d[TF{:}VII_a^m{:}ATIII]}{dt} = k_{42}[TF:VII_a^m][ATIII] \tag{4.34}$$

$$\frac{d[X_a^m]}{dt} = \begin{array}{l} k_{10}^{on}[X_a](p_{10} - e_{10}^{mtot} - z_{10}^{mtot}) - k_{10}^{off}[X_a^m] - k_{28}[X_a^m][V_a^m] + k_{27}[X_a:V_a] \\ +k_{22}[IX_a:VIII_a:X^m] \end{array} \tag{4.35}$$

$$\frac{d[II_a^m]}{dt} = \begin{array}{l} k_2^{on}[II_a](p_2 - e_2^{mtot} - z_2^{mtot}) - k_2^{off}[II_a^m] \\ +k_{16}[X_a^m][II^m] + k_{32}[mII_a^m][X_a:V_a] \end{array} \tag{4.36}$$

$$\begin{aligned}\frac{d[X^m]}{dt} = \; & k_{10}^{on}[X](p_{10} - e_{10}^{mtot} - z_{10}^{mtot}) - k_{10}^{off}[X^m] - k_{21}[IX_a : VIIIa][X^m] + \\ & k_{20}[IX_a : VIII_a : X^m] + k_{25}[IX_a : VIII_a : X^m]\end{aligned} \tag{4.37}$$

$$\frac{d[IX^m]}{dt} = k_9^{on}[X](p_9 - e_9^{mtot} - z_9^{mtot}) - k_9^{off}[IX^m] \tag{4.38}$$

$$\begin{aligned}\frac{d[IX_a^m]}{dt} = \; & k_9^{on}[IX_a](p_9 - e_9^{mtot} - z_9^{mtot}) - k_9^{off}[IX_a^m] \\ & -k_{19}[VIII_a^m][IX_a^m] + k_{18}[IX_a : VIII_a] + k_{25}[IX_a : VIII_a : X] + \\ & k_{25}[IX_a : VIII_a]\end{aligned} \tag{4.39}$$

$$\begin{aligned}\frac{d[II^m]}{dt} = \; & k_2^{on}[II](p_2 - e_2^{mtot} - z_2^{mtot}) - k_2^{off}[II^m] \\ & -k_{16}[X_a^m][II^m] - k_{30}[X_a : V_a][II^m] + k_{29}[X_a : V_a : II^m]\end{aligned} \tag{4.40}$$

$$\frac{d[VIII^m]}{dt} = \; k_8^{on}[VIII](p_8 - e_8^{mtot} - z_8^{mtot}) - k_8^{off}[VIII^m] \tag{4.41}$$

$$\begin{aligned}\frac{d[VIII_a^m]}{dt} = \; & k_8^{on}[VIII_a](p_8 - e_8^{mtot} - z_8^{mtot}) - k_8^{off}[VIII_a^m] \\ & -k_{19}[VIII_a^m][IX_a^m] + k_{18}[IX_a : VIII_a] \\ & -k_{17}^{+}[APC][VIII_a^m] + (k_{17}^{+} + k_{17}^{cat})[APC : VIII_a^m]\end{aligned} \tag{4.42}$$

$$\frac{d[V^m]}{dt} = \; k_5^{on}[V](p_5 - e_5^{mtot} - z_5^{mtot}) - k_5^{off}[V^m] \tag{4.43}$$

$$\begin{aligned}\frac{d[V_a^m]}{dt} = \; & k_5^{on}[V_a](p_5 - e_5^{mtot} - z_5^{mtot}) - k_5^{off}[V_a^m] \\ & -k_{28}[X_a^m][V_a^m] + k_{27}[X_a : V_a] \\ & -k_{16}^{-}[APC][V_a^m] + (k_{16}^{-} + k_{16}^{cat})[APC : V_a^m]\end{aligned} \tag{4.44}$$

$$\begin{aligned}\frac{d[mII_a^m]}{dt} = \; & k_2^{on}[mII_a](p_2 - e_2^{mtot} - z_2^{mtot}) - k_2^{off}[mII_a^m] \\ & -k_{32}[mII_a^m][X_a : V_a] + k_{31}[X_a : V_a : II^m]\end{aligned} \tag{4.45}$$

$$\begin{aligned}\frac{\partial[II_a^{EC}]}{\partial t} + \mathbf{u_0} \cdot \nabla[II_a^{EC}] = \; & D_{(diff,II_a^{EC})}([II_a] - [II_a^{EC}]) - \\ & k_{tm}^{on}[II_a^{EC}]([TM] - [TM : II_a] - [TM : II_a : PC]) \\ & + k_{tm}^{off}[TM : II_a]\end{aligned} \tag{4.46}$$

$$\begin{aligned}\frac{d[TM:II_a]}{dt} = \; & k_{tm}^{on}[II_a^{EC}]([TM] - [TM : II_a] - [TM : II_a : PC]) - k_{tm}^{off}[TM : II_a] \\ & -k_{pc}^{+}[TM : II_a][PC] + (k_{pc}^{-} + k_{pc}^{cat})[TM : II_a : PC]\end{aligned} \tag{4.47}$$

$$\frac{d[TM:II_a:PC]}{dt} = \; k_{pc}^{+}[TM : II_a][PC] - (k_{pc}^{-} + k_{pc}^{cat})[TM : II_a : PC] \tag{4.48}$$

$$\begin{aligned}\frac{\partial[APC^{EC}]}{\partial t} + \mathbf{u_0} \cdot \nabla[APC^{EC}] = \; & D_{(diff,APC^{EC})}([APC] - [APC^{EC}]) + \\ & k_{pc}^{cat}[TM : II_a : PC]\end{aligned} \tag{4.49}$$

$$\begin{aligned}\frac{\partial[APC]}{\partial t} + \mathbf{u} \cdot \nabla[APC] = \; & -D_{(diff,APC^{EC})}([APC] - [APC^{EC}]) \\ & -k_{16}^{-}[APC][V_a^m] + (k_{16}^{-} + k_{16}^{cat})[APC : V_a^m] \\ & -k_{17}^{+}[APC][VIII_a^m] + (k_{17}^{+} + k_{17}^{cat})[APC : VIII_a^m]\end{aligned} \tag{4.50}$$

4.2 Numerical methods for solving model equations

The 2D NS equations are solved by using the projection method. The convection-reaction-diffusion equations are solved by an operator splitting scheme. The convection and diffusion components of each chemical equation is firstly solved by a Crank-Nicolson time discretization scheme. Then reaction components of these partial differential chemical equations are solved together with the chemical ODEs. To compute advective terms $[\mathbf{u} \cdot \nabla[\ ]]^{n+1/2}$ in these chemical PDEs, the fluid velocity is needed. For this reason, NS Equations and PDE type chemcial reaction equations are solved together.

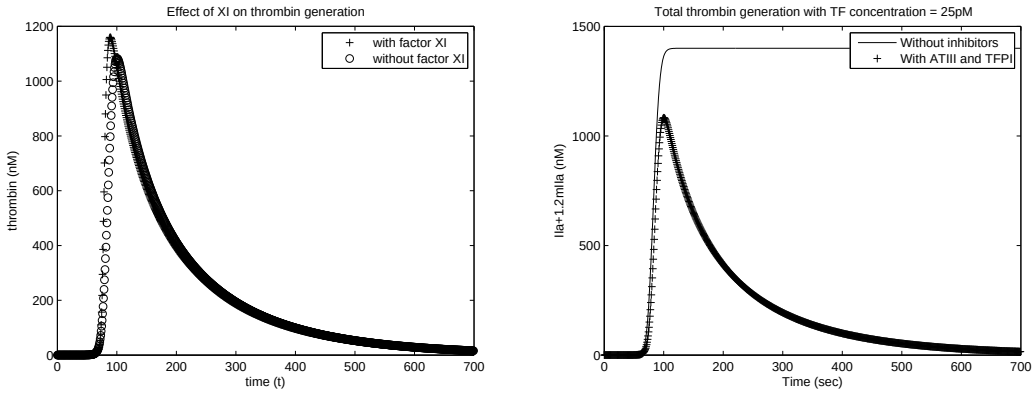

(a) (b)

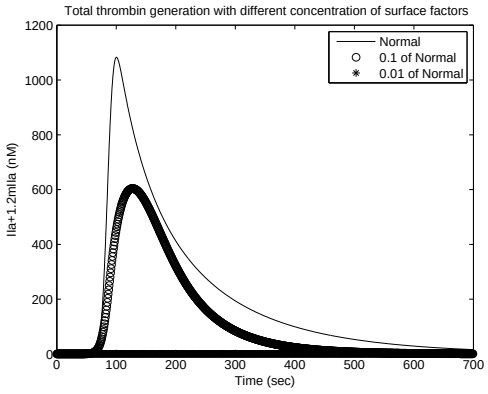

(c)

Figure 2: a) Effect of the FXI on thrombin generation. (b) Total thrombin amount generated (thrombin (IIa) + meizothrombin (mIIa)) with concentration of TF = 25 pM. The solid line represents total thrombin generation without inhibitors ATIII and TFPI. the line with cross (+) represents total thrombin generation with inhibitors. Factor XI is included. (c) Total thrombin amount generated (thrombin (IIa) + meizothrombin (mIIa)) with concentration of surface binding sites = 1.0, 0.1, 0.01 of normal concentration respectively.

4.3 Calibration of the coagulation sub-model

After adding factor XI (FXI) to the Kenneth Mann's model (modified ODEs model) we found that it modestly promoted thrombin generation and that thrombin concentration reached a slightly higher peak at an earlier time (see Figure 2(a)). These results are consistent with in vitro measurements of coagulation assays and clinical observation that FXI deficient individuals experience only minor bleeding problems.

After comparing Figure 2(b), obtained using modified ODE model, with Figure 2 from (6), we conclude that modified ODEs model is quantitatively identical to Mann's coagulation model in the static environment except for producing an earlier peak time in thrombin generation due to FXI. Therefore, we were able to estimate values of volume concentration of binding sites for surface factors by adjusting numbers of surface binding sites in the modified ODEs model to obtain production rate of thrombin similar to that of the original Mann's model in the static environment. Notice that concentration of surface binding sites exhibits threshold effects. Figure 2(c) shows simulation results obtained using modified ODEs model for different numbers of binding sites. Generation of thrombin is negligible in case of 1% of normal concentration of surface binding sites.

References

1. Anderson, A.R.A, Chaplain, M.A.J. & Rejniak, K.A. Single-Cell-Based Models in Biology and Medicine, Birkhaauser Basel; (July 2007)

2. Chaturvedi R., Huang C., Kazmierczak B., Schneider T., Izaguirre J.A., Glimm T., Hentschel H.G., Glazier J.A., Newman S.A., Alber M.S. 2005 On multiscale approaches to three-dimensional modelling of morphogenesis. *Journal of the Royal Society, Interface/the Royal Society* 2, 237-253

3. Chen N, Glazier JA, Izaguirre JA, Alber MS. 2007. A parallel implementation of the Cellular Potts Model for simulation of cell-based morphogenesis. *Computer physics communications* 176, 670–681.

4. Chen, D.Z., M.H. Smid, and B. Xu. 2005 Geometric algorithms for density-based data clustering. *International Journal of Computational Geometry and Applications*, 15(3), 239–260.

5. Christley, S., M. Alber, and S.A. Newman. 2007 Patterns of mesenchymal condensation in a multiscale, quasi-3D discrete stochastic model. *PLoS Computational Biology* **3** 4, e76.

6. Hockin, M., K. Jones and K. Mann. A model for the stoichiometric regulation of blood coagulation. *J. of Biological Chemistry*, 277:18322–18333, 2002.

7. Knewitz, M.A. & Mombach, J.C.M. 2006 Computer simulation of the influence of cellular adhesion on the morphology of the interface between tissues of proliferating and quiescent cells. *Comput Biol Med* **36**(1), 59–69

8. Merks R.M., Brodsky S.V., Goligorksy M.S., Newman S.A., Glazier J.A. 2006 Cell elongation is key to in silico replication of in vitro vasculogenesis and subsequent remodeling. *Developmental biology* 289, 44–54

9. Mu, J., X.-M. Liu, M.M. Kamocka, Z.-L. Xu, M.S. Alber, E.D. Rosen, and D.Z. Chen. Segmentation, Reconstruction, and Analysis of Blood Thrombi Formation in 2-Photon Microscopy Images, *EURASIP Journal on Advances in Signal Processing*, Vol. 2010, Article ID 147216, 8 pages, 2010. doi:10.1155/2010/147216 (to appear).

10. Mu, J., X.-M. Liu, M.M. Kamocka, Z.-L. Xu, M.S. Alber, E.D. Rosen, and D.Z. Chen. Segmentation, reconstruction, and analysis of blood thrombi in 2-photon microscopy images. *Proceedings of the 2009 22nd IEEE International Symposium on Computer-Based Medical Systems (CBMS)*, Albuquerque, NM, August 3-4, 2009, doi:10.1109/CBMS.2009.5255347, pp. 1-8.

11. Newman, M. & Barkema, G. 1999 In *Monte Carlo Methods in Statistical Physics*. Oxford University Press, Oxford

12. Otsu, N. A threshold selection method from gray-level histograms. *IEEE Trans. Systems, Man, and Cybernetics*, 9:62-66, 1979.

13. Sozinova, O., Jiang, Y., Kaiser, D. & Alber, M. A three-dimensional model of myxobacterial fruiting-body formation. *Proc Natl Acad Sci U S A* **103** (46), 17255–17259, 2006.

14. Wu, Y., Jiang, Y., Kaiser, D., and M. Alber. 2009 Periodic reversal of direction allows Myxobacteria to swarm. *Proc Natl Acad Sci U S A* **106** (4), 1222-1227 (featured in the Nature News, January 20th, 2009, doi:10.1038/news.2009.43).